Phase transformations upon doping in WO_3

Wennie Wang,[a] Anderson Janotti,[b] and Chris G. Van de Walle
Materials Department, University of California, Santa Barbara, California 93106-5050, USA

(Received 8 March 2017; accepted 11 May 2017; published online 7 June 2017)

High levels of doping in WO_3 have been experimentally observed to lead to structural transformation towards higher symmetry phases. We explore the structural phase diagram with charge doping through first-principles methods based on hybrid density functional theory, as a function of doping the room-temperature monoclinic phase transitions to the orthorhombic, tetragonal, and finally cubic phase. Based on a decomposition of energies into electronic and strain contributions, we attribute the transformation to a gain in energy resulting from a lowering of the conduction band on an absolute energy scale. *Published by AIP Publishing.* [http://dx.doi.org/10.1063/1.4984581]

I. INTRODUCTION

Tungsten trioxide (WO_3) has a variety of applications, including in gas sensors,[1] as a photocatalyst for water splitting,[2] and as electrochromic films in smart windows.[3,4] As an electrochromic film, the optical transmittance decreases with higher levels of doping and the material colors from transparent to blue. WO_3 has an ABO_3 perovskite structure with a vacant A site, enabling high levels of doping up to stoichiometric compositions.[5] Monovalent species, such as H, Li, and Na, are commonly used as dopants due to their fast diffusivities. At increasingly high doping levels, WO_3 has been observed to undergo structural changes to higher symmetry phases.[5–9] The ability to dope with a variety of foreign species makes the structure and electronic properties of WO_3 highly tunable.

At room temperature, WO_3 is monoclinic, with off-centered W ions surrounded by oxygen atoms in distorted octahedra. As a function of doping, the highly distorted monoclinic phase transforms to a tetragonal, and ultimately to a cubic structure.[7] These transformations have been experimentally observed upon doping with Na[5,8] and Li.[9] A study from Wang *et al.* used *in situ* transition electron microscopy to investigate the kinetics of dopant intercalation and structural transformation in Li-intercalated WO_3.[10] Several computational studies have investigated the influence of doping in WO_3. One such study compared and contrasted the electronic structure and bonding environment of ReO_3 with $NaWO_3$, which are isoelectronic.[11] Another study showed that the relaxed volume increases and the bandgap decreases with the size of the dopant at low doping concentrations (~4%).[12] Walkingshaw *et al.* demonstrated, using density functional theory in the local density approximation (LDA), that the structural transformations could be decomposed into certain modes of distortion (e.g., changes of bond length in the *xy*-plane).[13] However, the physical mechanisms of this structural transformation have not yet been fully explained.

In the present work, we distill the observed structural transformations to adding excess electrons to the system and elucidate the mechanisms of the structural phase transformations using density functional theory with a hybrid functional. We perform a detailed analysis of charge doping up to stoichiometric concentrations to understand the driving force for the structural transformation. We quantify the energetics of the transformation and demonstrate that the lowering of the conduction bands between the monoclinic and higher symmetry phases is the energetic driving force.

Experimentally, the addition of electrons is achieved by doping with alkali atoms;[5,8,9] it could also be associated with the presence of oxygen vacancies.[14] Explicit inclusion of dopants or point defects in our calculations could affect the quantitative results and shift the computationally determined phase boundaries. Consideration of dopant-specific effects is beyond the scope of the present work; the complexity of that problem is illustrated by the differences observed between experimental results that nominally use the same dopant (e.g., Na in Refs. 8 and 15). Our goal in the present paper is to show that essential physics is captured by focusing on the addition of excess electrons.

II. COMPUTATIONAL METHODOLOGY

Our calculations are based on (generalized) Kohn-Sham theory[16] using projector-augmented wave, pseudopotentials,[17] as implemented in the Vienna *Ab initio* Simulation Package (VASP).[18,19] For W, the 5*d* and 6*s* states are treated as valence states; for O, the valence states are the 2*s* and 2*p* states. We use the hybrid functional of Heyd, Scuseria, and Ernzerhof (HSE),[20,21] which mixes the short-range PBE exchange with the screened Hartree-Fock exchange. The HSE mixing parameter is chosen to be the standard 25%.

We choose the primitive 32-atom unit cell of the room-temperature (RT) monoclinic phase (containing 8 W atoms). Figure 1 shows this monoclinic structure as well as the tetragonal, orthorhombic, and cubic unit cells. Varying degrees of octahedral distortion and cation off-centering occur, with the cubic phase having no distortions and being highest in symmetry. We used a $4 \times 4 \times 4$ Γ-centered *k*-point mesh. We

[a]Electronic mail: www.ennie@engineering.ucsb.edu
[b]Present address: Materials Science and Engineering Department, University of Delaware, Newark, Delaware 19716-1501, USA.

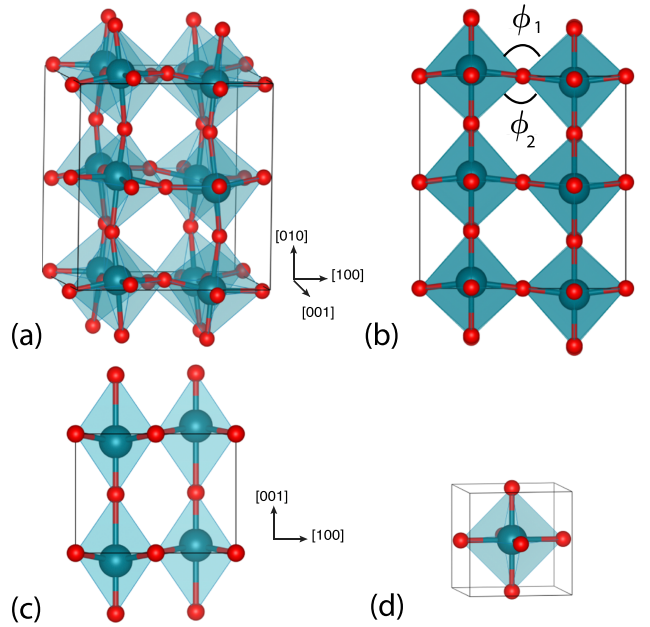

FIG. 1. Unit cells of WO_3 in order of increasing symmetry: (a) room-temperature (RT) monoclinic (space group $P2_1/c$), (b) orthorhombic (*Pbcn*), (c) tetragonal (*P4/nmm*), and (d) cubic ($Pm\bar{3}m$). An example of the relative tilt angles ϕ_1 and ϕ_2 along $\hat{x}$ between octahedra is indicated; the tilt angles are similarly defined for $\hat{y}$ and $\hat{z}$.

tested k-point meshes up to $8 \times 8 \times 8$ and found that lattice parameters changed by less than 0.25%, volumes by less than 0.5%, and relevant energy differences by less than 15 meV per formula unit. All calculations had a plane-wave basis set energy cutoff of 500 eV.

The majority of our calculations are performed for pure charge doping, i.e., no dopant atoms are included and only electrons are added to the system. At least one point is calculated for every increment of $x = 0.0625$ electrons per formula unit up until $x = 0.75$, beyond which no further phase changes occur. A homogeneous compensating background provides charge neutrality as it is standard practice in first-principles calculations for charged systems.[22] In the real system, the electrons would be supplied by dopant atoms that become ionized, and these positive ions provide the compensating charge. Each calculation is initiated with the 32-atom RT monoclinic phase of WO_3 with a given amount of electron charge added. All calculations are converged until the residual forces are below 0.05 eV/Å, at which point the symmetry of the final structure is determined.

III. RESULTS AND DISCUSSION

A. Investigation of bulk WO_3

We begin with a description of the bulk phases of WO_3. Different phases of WO_3 differ by the extent to which the oxygen octahedra are distorted and the W atoms are off-centered in the octahedra, as shown in the unit cells in Fig. 1. In the cubic phase, the W ions are centered in straight, upright octahedra of oxygen atoms. In the tetragonal structure, the W ions are displaced in an alternating pattern along the [001] and [00$\bar{1}$] directions while the octahedra remain upright. In the orthorhombic phase, the tilting of the octahedra (i.e., ϕ_1 and ϕ_2) along $\hat{x}$ and $\hat{y}$ directions deviate from right angles and the W ions are offset from the center of the octahedra along non-Cartesian directions (e.g., [110]) in an alternating fashion. In the monoclinic phase, the W ions further displace along any direction, and the octahedra are free to rotate, tilt, and distort in all directions. The β angle may take on values different from 90° in the monoclinic phase, and is taken as the angle between the [100] and [001] lattice vectors. The rotations and tilts of octahedra corresponding to the symmetry of the crystallographic space groups within Glazer notation[23] are well-documented for perovskites,[24] including WO_3.[25] The progression of these distortions as observed during the phase transformations is described in detail in Sec. III B.

Our calculated lattice parameters and bandgaps for the unit cells of different phases shown in Fig. 1 are listed in Table I. The structural parameters as calculated with HSE compare well to experimental values. They also agree with the previous hybrid functional calculations[26] to within 0.5%. Electronic band structures for the different phases are shown in Fig. 2.

B. Phase diagram with electron doping

We first describe the structural changes associated with the phase transformation observed with electron doping, beginning with the monoclinic structure at low electron concentrations. We perform calculations at discrete values of electron concentrations and report the phase observed for the lowest-energy structure at each concentration. Due to this discrete sampling, the electron concentrations at which phase boundaries occur are approximate. As these structural transformations are gradual, the marked phase boundaries represent not a sudden change in structure, but a rough delineation between two observed phases. We note that similar issues arise in an experimental determination of phase boundaries. In our

TABLE I. Experimental and calculated lattice parameters and bandgaps for WO_3; "ind" indicates indirect, "dir" direct bandgaps. For calculated indirect gaps, the location of the valence-band maximum (VBM) and conduction-band minimum (CBM) in the Brillouin zone is indicated as (ind: VBM, CBM).

	a (Å)	b (Å)	c (Å)	β (°)	E_g (eV)
			RT Monoclinic, $P2_1/c$		
Expt.[a]	7.31	7.54	7.69	90.90	2.6-2.8 (ind)
HSE	7.41	7.63	7.79	90.15	2.56 (dir: Γ)
			Orthorhombic, *Pbcn*		
Expt.[b]	7.36	7.57	7.76	90.00	...
HSE	7.43	7.64	7.79	90.00	2.49
			Tetragonal, *P4/nmm*		
Expt.[c]	5.25	5.25	3.91	90.00	...
HSE	5.29	5.29	3.96	90.00	1.53 (ind: Z, Γ)
			Cubic, $Pm\bar{3}m$		
Expt.[d]	3.78	3.78	3.78	90.00	...
HSE	3.79	3.79	3.79	90.00	1.53 (ind: R, Γ)

[a]References 27–30.
[b]Reference 31.
[c]Reference 32.
[d]References 8 and 33.

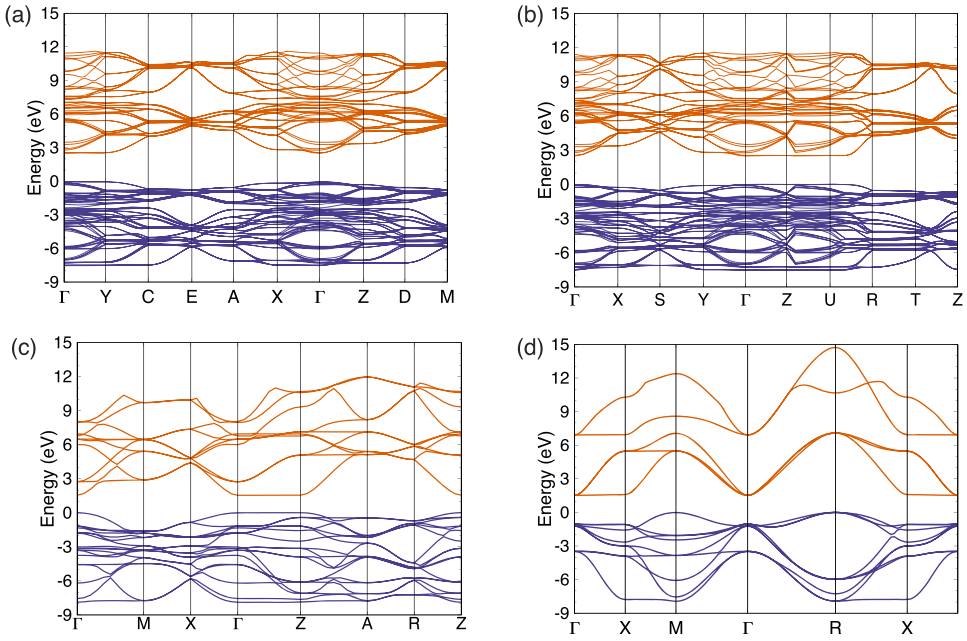

FIG. 2. Calculated band structures for different phases of WO_3: (a) room-temperature (RT) monoclinic, (b) orthorhombic, (c) tetragonal, and (d) cubic.

computational approach, we base the phase boundaries on a collective examination of the structural parameters (lattice parameters and internal distortion of atomic coordinates) described below. Phase boundaries are indicated as solid vertical lines in Figs. 3 and 4.

Figure 3 illustrates the evolution of the lattice parameters, β angle, and volume as a function of electron concentration. The figure tracks the progression from the low-symmetry monoclinic phase where $a \neq b \neq c$ and $\beta > 90^{\circ}$ to the high-symmetry cubic phase where lattice parameters become equivalent and β approaches 90°. The volume expansion shown in Fig. 3(c) is largely determined by the degree of tilting of the octahedra. A significant volume expansion occurs within the monoclinic phase upon addition of electrons, due to the decrease in the amount of tilting. Only a small amount of additional expansion occurs within the orthorhombic (*Pbcn*) and tetragonal ($P4/nmm$) phases.

The distortions of the internal coordinates are shown in Fig. 4. A useful metric for the overall distortion of the octahedra is the mean of the quadratic elongation parameter,[34]

$$\langle \lambda_{oct} \rangle = \sum_{i=1}^{6} \frac{1}{6} \left(\frac{l_i}{l_0} \right)^2 , \tag{1}$$

where l_0 is the bond length of the pseudocubic structure with the volume of the distorted perovskite and l_i is an actual bond length of the distorted perovskite; λ_{oct} is a measure of the distortedness of a perovskite from a cubic symmetry and is thus unity for the cubic phase. As shown in Fig. 4(a), the quadratic elongation parameter approaches unity as a function of doping when no distortions in bond lengths are present. The corresponding evolution of bond lengths illustrating the internal distortion of the octahedra along each direction is shown in Fig. 4(b).

The bond angle variance σ_θ^2, shown in Fig. 4(c), provides complementary information about the distortion of bond angles in an octahedron, and is defined as the variance from a right angle of the 12 O–W–O angles θ between adjacent O atoms within an octahedron,[34]

$$\sigma_\theta^2 = \sum_{i=1}^{12} \frac{1}{11} (\theta_i - 90^{\circ})^2 . \tag{2}$$

Finally, the relative tilt angles ϕ_1 and ϕ_2 between octahedra are reported in Fig. 4(d) along the $\hat{x}$, $\hat{y}$, and $\hat{z}$ directions.

The initially monoclinic structure of space group $P2_1/c$ symmetry persists up to around $x = 0.1875$, where x is defined as the number of electrons added per formula unit. Within this phase, the tilts of the octahedra decrease with increased doping, and the lattice parameters a and b converge [Fig. 3(a)]. Six distinct W–O bond lengths are present [Fig. 4(b)] due to the displacement of the W ion from the center of the octahedra. The smallest displacements occur along the $\hat{x}$ direction.

Between $x = 0.1875$ and $x = 0.25$, a transition to the orthorhombic *Pbcn* phase occurs, in which a and b are equal and the angle β approaches a right angle with increased doping. In the orthorhombic symmetry, octahedral rotations (i.e., tilts measured by ϕ) are reduced around the $\hat{x}$, $\hat{y}$, and $\hat{z}$ directions, with tilts in the $\hat{x}$ and $\hat{y}$ directions becoming equal. In terms of the W ions, the $\hat{y}$-direction displacements diminish, as evidenced in Fig. 4(b).

The *Pbcn* orthorhombic phase is present up to around $x = 0.3125$; a transition to the tetragonal $P4/nmm$ phase takes place between $x = 0.3125$ and $x = 0.375$. In going from the orthorhombic to tetragonal phases, the relative tilting between octahedra monotonically decreases [Fig. 4(d)]. With increased doping in the tetragonal phase, the lattice parameter c approaches $a = b$. The $\hat{x}$- and $\hat{y}$-displacements of the W ions also vanish, as shown in Fig. 4(b). This is also evident in the decrease of the bond angle variance, shown in Fig. 4(c). The remaining displacement of W ions along the $\hat{z}$−direction results in an antiferroelectric-like pattern, with alternating displacements in the $+\hat{z}$ and $-\hat{z}$ directions. With

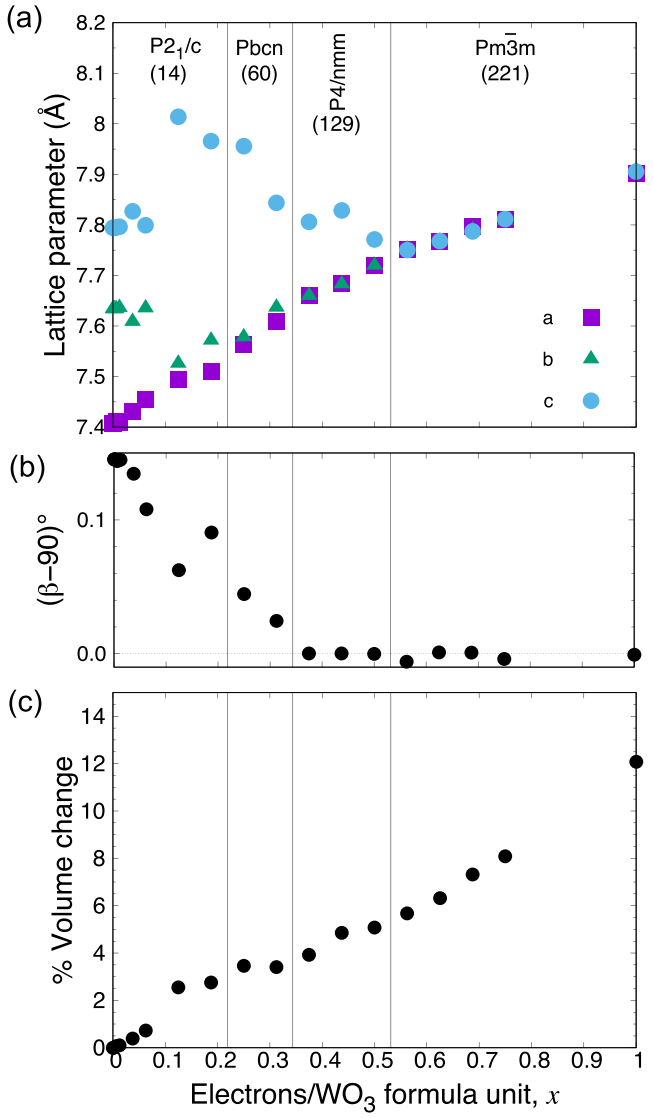

FIG. 3. Evolution of (a) lattice parameters, (b) β angle, and (c) volume as a function of electron doping in HSE. Space groups and space-group numbers for the various phases are indicated.

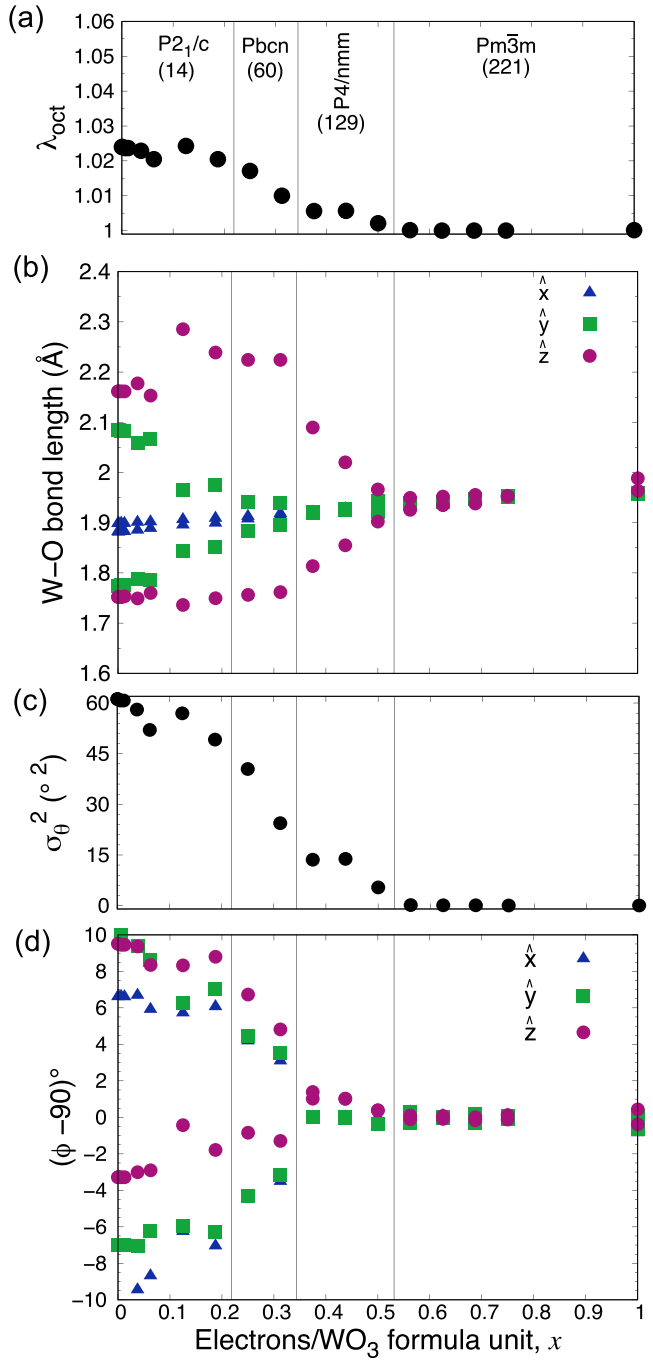

FIG. 4. Evolution of (a) the quadratic elongation λ_{oct}, (b) variation of W–O bond lengths, (c) bond angle variance σ_θ^2, and (d) tilt angles of octahedra ϕ_1 and ϕ_2 for each of the crystal directions as a function of electron doping with boundaries between symmetry phases (solid lines), as defined in the text. Space groups and space-group numbers for the various phases are indicated.

increasing doping, these bond lengths along the $\hat{z}$ direction become close to each other and to those in $\hat{x}\hat{y}$-plane.

The tetragonal *P4/nmm* phase is stable up to around $x = 0.5000$; then a transition to the cubic phase ($Pm\bar{3}m$ symmetry) takes place between $x = 0.5000$ and $x = 0.5625$. This is evident in Fig. 3(a), in which $a = b = c$, and in Fig. 4, where the quadratic elongation converges to unity, all W–O bonds converge to a single value, and the bond angle variance vanishes. Once the system is in the cubic phase, additional doping merely results in an expansion of the unit-cell volume [Fig. 3(a)].

C. Decomposition into strain and electronic energies

In order to elucidate the mechanisms driving the structural phase transformations, we decompose the total energy change into its strain and electronic components. Our first-principles methodology allows us to add or remove excess fractional electrons, and to include or exclude relaxation of lattice vectors and atomic positions. This yields four possible terms. We adopt the notation $E_y(x)$ to mean the total energy of a structure with an excess (fractional) concentration of electrons x in the conduction band, but with an atomic structure relaxed with y electrons in the conduction band. That is, the relaxed structure obtained with x electrons in the conduction band has energy $E_x(x)$, and the relaxed ground-state monoclinic phase with no excess doping has energy $E_0(0)$.

First, we add excess electrons to the system to obtain $E_0(x)$, the total energy of the system with extra electrons added, but with the atomic structure kept fixed to that of the

monoclinic (undoped) ground state. We can then relax the lattice vectors and atomic positions, leading to a relaxed structure with energy $E_x(x)$. At high enough doping, transformations to phases with higher symmetry will be observed, as discussed in Sec. III B. We define $E^{net}(x)$ as the energy difference between the relaxed system with x electrons and the unrelaxed system (i.e., fixed in the monoclinic structure) with x electrons,

$$E^{net}(x) = E_x(x) - E_0(x). \tag{3}$$

Our aim is to provide insight into the driving force for energy gain by decomposing this energy.

Once x electrons have been added and the structure is relaxed, we can consider this atomic structure, remove the excess electrons, and calculate the total energy of this structure, denoted $E_x(0)$. The difference between this energy and the energy of the undoped monoclinic structure provides a measure of the energy cost involved in deforming the structure; we will refer to this as "strain energy," $E^{strain}(x)$,

$$E^{strain}(x) = E_x(0) - E_0(0). \tag{4}$$

The fact that transformations to other structures take place at higher doping levels indicates that placing the electrons in the conduction band leads to an energy gain, which we will refer to as $E^{elec}(x)$. We decompose the energy $E^{net}(x)$ as follows:

$$E^{net}(x) = E^{strain}(x) + E^{elec}(x) \tag{5}$$

Combining Eqs. (3)–(5) leads to

$$\begin{aligned} E^{elec}(x) &= E^{net} - E^{strain} && \text{(6a)} \\ &= [E_x(x) - E_0(x)] - [E_x(0) - E_0(0)], \\ &= [E_x(x) - E_x(0)] - [E_0(x) - E_0(0)]\,. && \text{(6b)} \end{aligned}$$

The rearrangement of the terms provides insight into the physical origin of this "electronic energy." The first term in square brackets in Eq. (6b), $[E_x(x) - E_x(0)]$, is a measure of the change in energy associated with changes in the electronic structure upon adding x electrons (to a fixed atomic structure). However, to make this term meaningful, we need to define a reference energy for those electrons; this is encapsulated in the second term, $[E_0(x) - E_0(0)]$, which is the energy of adding x electrons to the fixed monoclinic structure.

Figure 5 shows the decomposition of the net energy into its strain and electronic components. The strain cost to transform to a higher-symmetry phase is more than compensated by the electronic energy gain.

For the strain energy, further insight is provided by decomposing the strain energy into contributions related to volume expansion and to displacement of atomic positions. The volumetric component can be determined by considering the total energies associated with doping the cubic phase. An analogous strain energy E^{strain}_{volume} is thus calculated as in Eq. (7), but taking the undoped cubic phase as the reference state. The remainder in the strain energy, labeled $E^{strain}_{disp}(x)$, is then attributed to the energy associated with non-hydrostatic changes in lattice

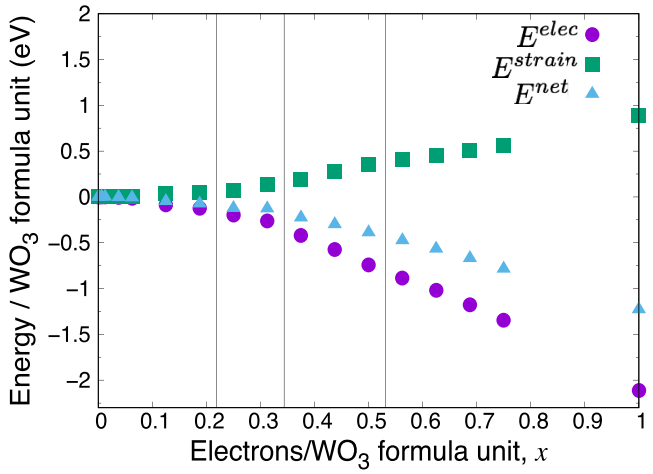

FIG. 5. Decomposition of energy into strain and electronic components, as described in the text.

vectors and with displacement of atomic positions,

$$\begin{aligned} E^{strain}(x) &= E_x(0) - E_0(0) \\ &= E^{strain}_{volume}(x) + E^{strain}_{disp}(x), && \text{(7a)} \\ E^{strain}_{volume}(x) &= [E^{cubic}_x(0) - E^{cubic}_0(0)], && \text{(7b)} \\ E^{strain}_{disp}(x) &= E^{strain}(x) - E^{strain}_{volume}(x), && \text{(7c)} \\ &= [E_x(0) - E_0(0)] - [E^{cubic}_x(0) - E^{cubic}_0(0)]. && \text{(7d)} \end{aligned}$$

Figure 6 shows this decomposition of the strain energy. Below the concentration for the onset of the cubic phase, the terms due to volumetric expansion and due to distortions contribute roughly equally to the overall strain. Once the cubic phase is reached, strain energy associated with distortions becomes constant and any additional strain energy is strictly due to volume expansion with additional electron doping.

D. Driving force for phase transformation

As shown in Secs. III A–III C, the transfer of the electron from the dopant to the host lattice leads to the structural transformations earlier characterized. We now demonstrate that the

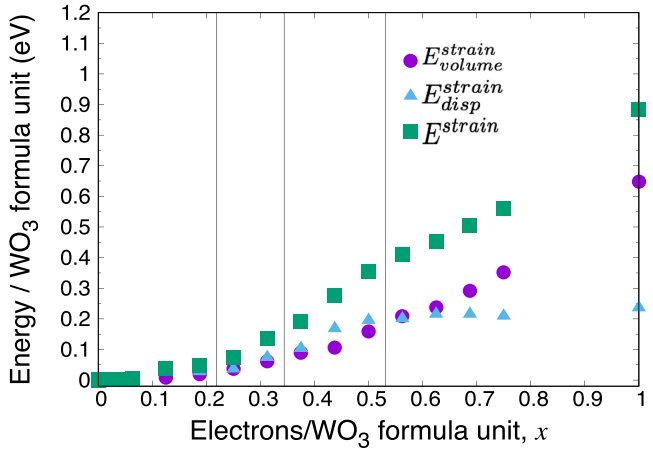

FIG. 6. Decomposition of strain energy into volumetric and internal displacement components.

gain in electronic energy, which drives the phase transformation (Fig. 5), is primarily due to a lowering of the conduction band on an absolute energy scale. Table I shows bandgaps for the various phases of WO_3. The higher the symmetry of the phase, the smaller is the bandgap. This trend can be attributed to the correlation between the bandwidth of the conduction band (composed primarily of W d states) and the degree of octahedral tilting and off-centering of W. Overlap between d orbitals is maximized in the highest-symmetry (cubic) structure. Strong overlap leads to large bandwidth and hence small bandgap. Lower-symmetry phases exhibit distortions of the octahedra that result in narrowed bandwidths and thus larger bandgaps. We explicitly demonstrate and quantify how distortions play a role in the phase transformations for electronically doped WO_3.

The overall change in the bandgap as a function of doping, going from $x = 0$ to $x = 1$ is $\Delta E_g = -1.45$ eV. To demonstrate that this change in gap is driven primarily by the structural distortions and only partially by volume expansion, we calculate the change in gap due to the individual contributions (without electron doping). We use the bandgap change observed for the expanded cubic phase as an indicator of what fraction of the bandgap change can be attributed to volume expansion. For the volume change corresponding to $x = 1$ [Fig. 3(c)], this yields a change in the bandgap of $\Delta E_g = -0.26$ eV. To determine how the bandgap changes with internal structural distortions, we introduce either just the tilting of the octahedra or only the offset of the W ions into the cubic structure at the (smaller) monoclinic volume. With only octahedral tilting, $\Delta E_g = -0.16$ eV; with only the offset of W ions, $\Delta E_g = -1.29$ eV; including both octahedral tilting and offset of W atoms of the monoclinic phase into the cubic structure, $\Delta E_g = -0.92$ eV. We note that the bandgap changes due to octahedral tilting, W offset, and volume change are not simply additive, since the various types of distortions interact. Still, these results indicate that while volume expansion does lead to a reduction in the bandgap, it is the structural distortions and in particular the offset of the W ions that are primarily responsible for the decrease in the bandgap.

While the change in bandgap is suggestive, we still need to demonstrate that the conduction band itself is lowered in energy. For that purpose we calculate the alignment of band structures between the cubic and monoclinic phases. In principle this requires a calculation for an interface between the two phases.[35,36] Such a calculation should be performed on a superlattice containing layers of each phase, which allows determining the alignment of the average electrostatic potentials within each phase. The position of the CBM with respect to the average electrostatic potential $\widetilde{V}$ is obtained from separate calculations of the bulk phases. Combining the superlattice with the bulk results yields the conduction-band offset.

Unfortunately, constructing a pseudomorphic interface between the cubic and monoclinic structures is challenging. The distortions of the monoclinic phase lead to disparate bond lengths at the cubic-monoclinic interface that result in dipoles, which makes extracting a meaningful average electrostatic potential difficult. We therefore make the plausible assumption that the change in average electrostatic potential between monoclinic and cubic depends primarily on volume, and contributions related to additional distortions of the cell and to changes in internal coordinates can be neglected. Based on this assumption, the average electrostatic potentials $\widetilde{V}$ in the cubic phase is equal to the average electrostatic potential in the monoclinic phase if the cubic phase is strained (expanded) to be at the same volume as the monoclinic phase. To obtain the alignment between the strained and unstrained cubic phase, we perform a calculation for a superlattice in which one layer consists of cubic material at its equilibrium volume, and the other layer is strained to reflect the volume change between cubic and monoclinic phases. This calculation yields the result that the average electrostatic potential in cubic WO_3 at its equilibrium volume is 0.16 eV lower than in cubic WO_3, which is expanded to match the volume of the monoclinic structure.

Figure 7 shows the resulting alignment of the electrostatic potential as well as the position of the CBM and the VBM referenced to the average electrostatic potential in the monoclinic and cubic phases. The resulting conduction-band offset between the cubic and monoclinic phases is 1.05 eV. The corresponding valence-band offset is much smaller, 0.02 eV. The insensitivity of the valence-band offset to the difference in structure between the cubic to monoclinic phases can be attributed to the fact that the O $2p$ states at the VBM are composed of non-bonding oxygen p-states,[37] which are relatively unaffected by distortions.

We note that the bandgap difference between the monoclinic and cubic phases reported in Fig. 7 is different from the value $\Delta E_g = -1.45$ eV reported above for the difference between $x = 0$ and $x = 1$. The difference is due to the fact that the bandgap for the cubic phase in Fig. 7 is for the undoped cubic phase at its equilibrium volume (as also reported in Table I), while the bandgap for $x = 1$ reflects the presence of a large concentration of electrons, leading to a volume expansion as well as additional conduction-band lowering due to bandgap renormalization. The purpose of Fig. 7 was

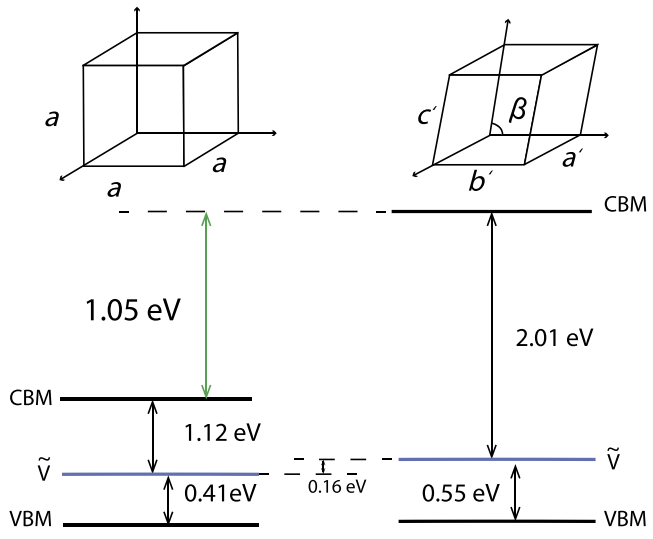

FIG. 7. Band alignment between the cubic and monoclinic phases of WO_3. The positions of the VBM and CBM are shown with respect to the average electrostatic potential $\widetilde{V}$ in each phase.

to demonstrate that the CBM of the cubic phase is significantly lower than that of the monoclinic phase, providing a driving force for the phase transition to the higher-symmetry structure when electrons are placed in the conduction band.

E. Comparison with previous work and with experiment

Walkingshaw *et al.*[13] also investigated how electronic doping of WO_3 leads to phase transformations. They focused on an examination of structural distortions rather than energetics. While the trends in modes of distortion upon electron doping are broadly similar to the ones found in our work, significant quantitative differences are evident for lattice parameters and atomic positions. The phase boundaries found by Walkingshaw *et al.*[13] also occur at much higher doping levels than in our study; for instance, the boundary between the tetragonal and cubic phase occurs at $x = 0.68$ in Ref. 13 while we find it at around $x = 0.531\,25$. We attribute these differences mainly to their use of the LDA. The electronic structure obtained with the HSE functional used in our work is known to be much more accurate than that obtained with LDA.[38,39] Lattice parameters, and hence volume, are significantly underestimated in LDA. A smaller volume corresponds to greater octahedral tilting, and thus lower-symmetry phases will appear stable up to higher electron concentrations in LDA calculations.

Computations with electron doping were also performed by Wang *et al.*,[10] who report phase boundaries at smaller electron concentrations. Again, the difference can be attributed to the use of a less accurate functional. Using GGA + U, Wang *et al.*[10] found lattice parameters for the monoclinic phase ($a = 7.68, b = 7.70, c = 7.76$ Å) that are significantly larger than those found experimentally or found with HSE (see Table I). By similar logic as in the comparison with the work of Walkingshaw *et al.*,[13] a larger volume corresponds to smaller octahedral distortions, and this will tend to stabilize higher-symmetry phases at smaller electron concentrations. Given the importance of electronic effects in driving the phase transitions (see Sec. III D), our results can be considered more reliable.

We now turn to a comparison with experiment. Zhong *et al.*[9] investigated charging with Li and reported that the phase boundaries observed in the case of charging differed significantly from those found in the case of discharging. Ranges of overlap were interpreted as regions of two-phase coexistence, but kinetic effects may also be playing a role. A comparison with our results, which are based purely on equilibrium energies, can therefore be only qualitative. The experimentally observed ranges of stability for different phases in the case of Li charging were $x \leq 0.015$ for monoclinic, $0.078 \leq x \leq 0.12$ for tetragonal, and $x \geq 0.21$ for cubic; in the case of discharging, the ranges were $x \leq 0.01$ for monoclinic, $0.08 \leq x \leq 0.13$ for tetragonal, and $x \geq 0.36$ for cubic, with the measurements going up to $x = 0.50$.[9] Other experiments were performed with Na:[8,15] Brown and Banks[8] observed the cubic phase for electron concentrations of $x \geq 0.26$, whereas Egdell and Hill[15] found that for $0.26 \leq x \leq 0.40$ other phases were present along with the cubic phase.

The difference between experimentally and computationally determined phase boundaries may be attributed to several factors. First, our calculations describe the behavior of bulk single crystalline material. This is not necessarily the case for experimental samples, which may be polycrystalline, contain impurities other than the intercalated species, or be subject to stress due to thin-film preparation.[7,9,15] We note that even studies that use the same dopant species (e.g., the Na-doping experiments in Refs. 8 and 15) report significant differences in the observed phase boundaries. Last but not least, our study was conducted for pure electron doping and did not consider the influence of dopants explicitly.

IV. CONCLUSIONS

We have performed a comprehensive first-principles treatment of the structural transformation of tungsten trioxide (WO_3) as a function of electron doping using hybrid functionals. A decomposition of energies into strain and electronic energies sheds light on the physical mechanisms underlying the transformations. We demonstrated that the structural transformation to higher-symmetry phases is driven predominantly by the lowering of the conduction band which occurs as structural distortions become smaller.

ACKNOWLEDGMENTS

We thank B. Himmetoglu, C. E. Dreyer, and K. Krishnaswamy for fruitful discussions. This work was supported by the U.S. Department of Energy, Office of Science, Basic Energy Sciences, under Award No. DE-FG02-07ER46434. W.W. acknowledges a Graduate Research Fellowship from the National Science Foundation under Grant No. DGE 1144085. Computational resources were provided by the Center of Scientific Computing at the CNSI and MRL (an NSF MRSEC and Grant No. DMR-1121053) (NSF CNS-0960316); this work also used the Extreme Science and Engineering Discovery Environment (XSEDE), which is supported by the National Science Foundation, Grant No. ACI-1053575 and the DOD High Performance Computing Modernization Program at Air Force Research Laboratory (Project No. ONRDC36953418).

[1] M. Penza, M. Tagliente, L. Mirenghi, C. Gerardi, C. Martucci, and G. Cassano, Sens. Actuators, B **50**, 9 (1998).
[2] R. Liu, Y. Lin, L. Y. Chou, S. W. Sheehan, W. He, F. Zhang, H. J. M. Hou, and D. Wang, Angew. Chem., Int. Ed. **50**, 499 (2011).
[3] C. Yang, J.-F. Chen, X. Zeng, and D. Cheng, Nanotechnology **27**, 75203 (2016).
[4] C. G. Granqvist, Sol. Energy Mater. Sol. Cells **60**, 201 (2000).
[5] R. Clarke, Phys. Rev. Lett. **39**, 1550 (1977).
[6] Z. Li, S. Wu, Z. Wang, and Y. Fu, J. Alloys Compd. **672**, 155 (2016).
[7] S.-H. Lee, M. J. Seong, H. M. Cheong, E. Ozkan, E. C. Tracy, and S. K. Deb, Solid State Ionics **156**, 447 (2003).
[8] B. Brown and E. Banks, J. Am. Chem. Soc. **76**, 963 (1954).
[9] Q. Zhong, J. R. Dahn, and K. Colbow, Phys. Rev. B **46**, 2554 (1992).
[10] Z. Wang, Y. He, M. Gu, Y. Du, S. X. Mao, and C. Wang, ACS Appl. Mater. Interfaces **8**, 24567 (2016).
[11] F. Cora, M. Stachiotti, C. Catlow, and C. Rodriguez, J. Phys. Chem. B **101**, 3945 (1997).
[12] S. Tosoni, C. Di Valentin, and G. Pacchioni, J. Phys. Chem. C **118**, 3000 (2014).
[13] A. Walkingshaw, N. Spaldin, and E. Artacho, Phys. Rev. B **70**, 165110 (2004).

[14]W. Wang, A. Janotti, and C. G. Van de Walle, J. Mater. Chem. C **4**, 6641 (2016).
[15]R. Egdell and M. Hill, Chem. Phys. Lett. **85**, 140 (1982).
[16]W. Kohn and L. J. Sham, Phys. Rev. **140**, A1133 (1965).
[17]P. E. Blöchl, Phys. Rev. B **50**, 17953 (1994).
[18]G. Kresse and D. Joubert, Phys. Rev. B **59**, 1758 (1999).
[19]G. Kresse and J. Furthmüller, Phys. Rev. B **54**, 11169 (1996).
[20]J. Heyd, G. E. Scuseria, and M. Ernzerhof, J. Chem. Phys. **118**, 8207 (2003).
[21]J. Heyd, G. E. Scuseria, and M. Ernzerhof, J. Chem. Phys. **124**, 219906 (2006).
[22]C. Freysoldt, B. Grabowski, T. Hickel, J. Neugebauer, G. Kresse, A. Janotti, and C. G. Van de Walle, Rev. Mod. Phys. **86**, 253 (2014).
[23]A. M. Glazer, Acta Crystallogr., Sect. B: Struct. Crystallogr. Cryst. Chem. **28**, 3384 (1972).
[24]M. A. Islam, J. M. Rondinelli, and J. E. Spanier, J. Phys.: Condens. Matter **25**, 175902 (2013).
[25]A. Garg, "Growth and characterization of epitaxial oxide thin films," Ph.D. thesis, University of Cambridge, 2001.
[26]F. Wang, C. Di Valentin, and G. Pacchioni, J. Phys. Chem. C **115**, 8345 (2011).
[27]R. Sivakumar, R. Gopalakrishnan, M. Jayachandran, and C. Sanjeeviraja, Opt. Mater. **29**, 679 (2007).
[28]F. P. Koffyberg, K. Dwight, and A. Wold, Solid State Commun. **30**, 433 (1979).
[29]G. Hodes, D. Cahen, and J. Manassen, Nature **260**, 312 (1976).
[30]R. D. Bringans, H. Höchst, and H. R. Shanks, Phys. Rev. B **24**, 3481 (1981).
[31]T. Vogt, P. M. Woodward, and B. A. Hunter, J. Solid State Chem. **144**, 209 (1999).
[32]W. L. Kehl, R. G. Hay, and D. Wahl, J. Appl. Phys. **23**, 212 (1952).
[33]W. A. Crichton, P. Bouvier, and A. Grzechnik, Mater. Res. Bull. **38**, 289 (2003).
[34]K. Robinson, G. V. Gibbs, and P. H. Ribbe, Science **172**, 567 (1971).
[35]C. G. Van De Walle and R. M. Martin, Phys. Rev. B **34**, 5621 (1986).
[36]L. Bjaalie, B. Himmetoglu, L. Weston, A. Janotti, and C. G. Van De Walle, New J. Phys. **16**, 025005 (2014).
[37]T. Wolfram and S. Ellialtioglu, *Electronic and Optical Properties of d-Band Perovskites*, 1st ed. (Cambridge University Press, Cambridge, UK, 2006), pp. 79–101.
[38]J. Paier, M. Marsman, K. Hummer, G. Kresse, I. C. Gerber, and J. G. Ángyán, J. Chem. Phys. **124**, 154709 (2006).
[39]J. Paier, M. Marsman, and G. Kresse, J. Chem. Phys. **127**, 024103 (2007).